Energy & Environmental Science

ROYAL SOCIETY OF CHEMISTRY

PAPER

View Article Online
View Journal | View Issue

Cite this: *Energy Environ. Sci.*, 2025, **18**, 10135

Cation-disordered rocksalt cathode for anode-free zinc-ion batteries

Zixuan Li, *[a] Rui Qi,[a] Yi Yuan,[ah] Lechen Yang,[a] Lijiang Song,[b] Ashok S. Menon,[cd] Louis F. J. Piper,[cd] Didier Wermeille,[ef] Paul Thompson,[ef] Robert A. House, *[a] Peter G. Bruce *[ag] and Alex W. Robertson *[h]

Received 13th May 2025,
Accepted 14th October 2025

DOI: 10.1039/d5ee02643a

rsc.li/ees

Aqueous zinc-ion batteries (ZIBs) suffer from sustained capacity loss at the zinc metal anode due to side reactions with the electrolyte, even under idle conditions. The concept of an anode-free ZIB would address this degradation by eliminating the metal anode source. A key requirement for such systems is a cathode that contains zinc in its pristine state and supports initial charging. Here, we report the synthesis and characterization of cation-disordered rocksalt (DRX) $ZnMnO_2$, a new cathode material suitable for anode-free ZIBs. $ZnMnO_2$ meets the essential criteria for anode-free operation of natively containing Zn in the pristine state, enabling an initial charge, as well as offering high initial charge capacity (312.8 mAh g^{-1}), and discharge voltage (1.36 V). We show that the dominant energy storage mechanism involves Mn dissolution and redeposition, with a smaller contribution arising from reversible Zn intercalation into a spinel phase that forms *in situ* during cycling. We further demonstrate the versatility of DRX cathodes by extending the concept to $ZnFeO_2$. These findings establish DRX materials as a promising platform for the development of cathodes suitable for anode-free ZIBs.

Broader context

Better rechargeable batteries are one of the essential technologies for the transition to a green economy, yet rechargeable batteries have a significant footprint in resource consumption and waste generation. The aqueous rechargeable zinc ion battery holds exciting potential as a truly sustainable battery technology, due to its aqueous electrolyte chemistry along with the relative abundance and recyclability of the principal metal components, zinc and manganese. An anode-free zinc-ion battery, which removes the excess of zinc typically employed at the anode in favour of just a bare current collector, would improve the cell's resilience to continued side-reaction losses at the anode (which occur even when the cell is not being cycled), thereby enhancing its shelf-life, and would also improve its energy density. While this anode-free concept has shown promise in lithium batteries, a challenge for zinc-ion batteries is that they lack an analogous range of quality cathode materials that natively host zinc, which is required for the first charge of an anode-free cell. Our submission reports the first synthesis of a family of zinc containing disordered rocksalt (DRX) materials, with the native zinc content allowing for anode priming during first charge when employed as a cathode in anode-free zinc-ion batteries.

Introduction

Aqueous zinc-ion batteries (ZIBs) have emerged as a promising energy storage technology owing to the abundance of zinc, the safety of aqueous electrolytes, and the high theoretical energy density of the Zn anode. The aqueous electrolyte offers inherent advantages, including fast ion diffusion and green chemistry. Conventional aqueous ZIBs batteries typically pair a Zn metal anode with a non-Zn-containing cathode such as MnO_2 or V_2O_5, forming a Zn/MnO_2 or Zn/V_2O_5 configuration.[1–4] However, even before electrochemical cycling, the presence of metallic Zn in contact with the aqueous electrolyte induces spontaneous parasitic reactions, including zinc corrosion, hydrogen evolution, and byproduct formation.[5] These side reactions cause

[a] *Department of Materials, University of Oxford, Parks Road, Oxford, OX1 3PH, UK. E-mail: zixuan.li@materials.ox.ac.uk, robert.house@materials.ox.ac.uk, peter.bruce@materials.ox.ac.uk*
[b] *Department of Chemistry, University of Warwick, Coventry, CV4 7AL, UK*
[c] *Warwick Manufacturing Group, University of Warwick, Coventry, CV4 7AL, UK*
[d] *The Faraday Institution, Quad One, Harwell Campus, Didcot, OX11 0RA, UK*
[e] *XMaS Beamline BM28, European Synchrotron Radiation Facility (ESRF), 71 Avenue des Martyrs, CS 40220, 38043 Cedex 9 Grenoble, France*
[f] *Department of Physics, University of Liverpool, Oliver Lodge, Oxford Street, Liverpool, L69 7ZE, UK*
[g] *Department of Chemistry, University of Oxford, Oxford, OX1 3QZ, UK*
[h] *Department of Physics, University of Warwick, Coventry, CV4 7AL, UK. E-mail: alex.w.robertson@warwick.ac.uk*

anode degradation, resulting in significant anode capacity loss and poor shelf life.[6] To offset this instability, conventional ZIBs often employ large excesses of Zn,[7] sometimes with N/P ratios exceeding 150, to compensate for corrosion-induced Zn loss, which masks the true degradation of the anode and reduces the practical energy density.[6–8]

While various mitigation strategies have been proposed, including artificial anode interface layers[9,10] and electrolyte additives[11,12] these approaches only suppress rather than eliminate the underlying issue. A more fundamental solution is to remove the zinc metal anode entirely, giving rise to the concept of an 'anode-free' ZIB.[13,14] In this configuration, a Zn-containing cathode is paired with a bare current collector, and zinc is electroplated onto the lightweight current collector during charging. As no metallic Zn is present during storage, parasitic reactions at the anode side are fundamentally avoided, thereby markedly enhancing the cell's shelf life. Additionally, replacing the heavy Zn metal with a lightweight current collector improves energy density.[15]

Realizing anode-free ZIBs requires cathodes that are intrinsically zinc-containing, enabling initial charging without preloading or external zinc sources. However, the main conventional ZIB cathodes, such as MnO_2,[1,2] and V_2O_5,[3,4] lack zinc in their pristine state, making them unsuitable for anode-free configurations. Existing zinc-containing cathodes, such as $ZnMn_2O_4$,[16,17] $Zn_3V_3O_8$,[18,19] $Zn_{0.56}VOPO_4{\cdot}2H_2O$,[20] $Zn_3V_4(PO_4)_6$,[21] $Zn_3[Fe(CN)_6]_2$,[22,23] $ZnMn_2(PO_4)_2$[24] and $Zn_2Mo_3O_8$,[25] often suffer from low voltage, poor capacity, or scalability issues. A greater range of zinc-containing cathodes is desirable to explore the viability of anode-free ZIBs as a potential strategy for combatting anode-side degradation.

In this work, we report the synthesis of $ZnMnO_2$ as a new ZIB cathode, which contains zinc in its pristine state and supports initial charging in an anode-free cell. This material is a type of cation-disordered rocksalt (DRX), which have shown promise in lithium-ion batteries due to their high capacity and limited volume change with cycling.[26] We show that the primary energy storage mechanism for this DRX cathode is Mn dissolution and redeposition; however, it also undergoes an irreversible phase transformation to a spinel structure during the first cycles of operation, which unlocks some reversible Zn^{2+} intercalation/deintercalation capacity.

To our knowledge, this is the first application of cation-disordered rocksalt materials in aqueous ZIBs, and opens the prospect for the development of new family of ZIB cathode materials. To demonstrate this, we also synthesized and explored DRX $ZnFeO_2$, utilizing an earth-abundant transition metal Fe, which yields promising performance. The ability of this series of DRX materials to be charged first, thanks to their intrinsic zinc content, provides a useful cathode option for anode-free zinc-ion batteries.

Results and discussion

There has been significant interest in cation-disordered rocksalt (DRX) materials as potential cathodes for lithium-ion batteries due to their offering a wide choice of transition metals and exhibiting high capacity.[26] In these materials, the random distribution of cations forms a network of low-barrier "0-TM" channels that allow Li ions to migrate through the anion sublattice *via* an octahedral–tetrahedral–octahedral pathway, enabling efficient and unconventional ion diffusion.[27] Moreover, the intrinsic cation disorder leads to small, isotropic volume changes during charge–discharge, helping to mitigate mechanical degradation over extended cycling.[26] These characteristics make DRX materials attractive for ZIBs as well. Various cations can be doped into Zn-based DRX systems, including Ni, Mg, Co, Fe, and Mn.[28] Among them, Mn was selected in this study due to its range of valence states, redox activity, natural abundance, and as its associated oxides typically exhibit high capacities and high operating voltages in aqueous ZIBs. The extensive research on Mn-based oxides in ZIB provides a solid foundation for further exploration, positioning Mn as a strong candidate for this study.

The cation-disordered rocksalt material $ZnMnO_2$ was synthesized using ZnO and MnO precursors. Offering a compatible rocksalt framework is crucial to allow ZnO to stabilize in the rocksalt structure under ambient pressure. MnO is an ideal dopant because of its rocksalt structure and the similar ionic radii of Mn^{2+} (0.82 Å) and Zn^{2+} (0.74 Å). The synthesis presents challenges due to the stability of ZnO's wurtzite structure. Previous studies have shown that transforming wurtzite ZnO into a rocksalt structure requires high pressure ($\sim$7 GPa) and high temperature (700 °C).[28,29]

The mixture of wurtzite ZnO and rocksalt MnO was ball-milled at 750 rpm for 8 hours using a Fritsch high-energy ball mill to form pure DRX $ZnMnO_2$. The high local heat and pressure generated during the ball milling process[30] are essential to induce the phase transformation of wurtzite ZnO into the rocksalt structure. The powder X-ray diffraction (XRD) pattern of the resulting DRX $ZnMnO_2$ material (Fig. 1a and Table S1) was analyzed using Rietveld refinement. The analysis confirmed that the material conforms to the $Fm\bar{3}m$ cubic rocksalt space group with no impurities and with a lattice parameter of 4.30 Å.

Pair distribution function (PDF) analysis of total X-ray scattering data was conducted for as-synthesized $ZnMnO_2$, as shown in Fig. 1b. While XRD provides information of the long-range structural ordering of $ZnMnO_2$, PDF analysis allows for examination of the local short-range structure at the atomic scale. The refined PDF data agrees well with the $Fm\bar{3}m$ space group of a disordered rocksalt structure across the entire range from 1 to 20 Å.

The spatial uniformity of the elemental distribution was confirmed by high-angle annular dark field scanning transmission electron microscopy (HAADF-STEM) with energy-dispersive X-ray spectroscopy (EDS) mapping (Fig. 1c). The elements Zn, Mn, and O are evenly distributed throughout the $ZnMnO_2$, with no evidence of segregation into other phases. The agglomerated particle sizes ranged from between 100 to 250 nm, as observed by scanning electron microscopy (SEM) imaging (Fig. S1a). High-resolution transmission electron microscopy (HRTEM) and its Fourier transform (Fig. S1b) revealed a lattice spacing of 2.5 Å, corresponding to the (111) plane. A selected area electron

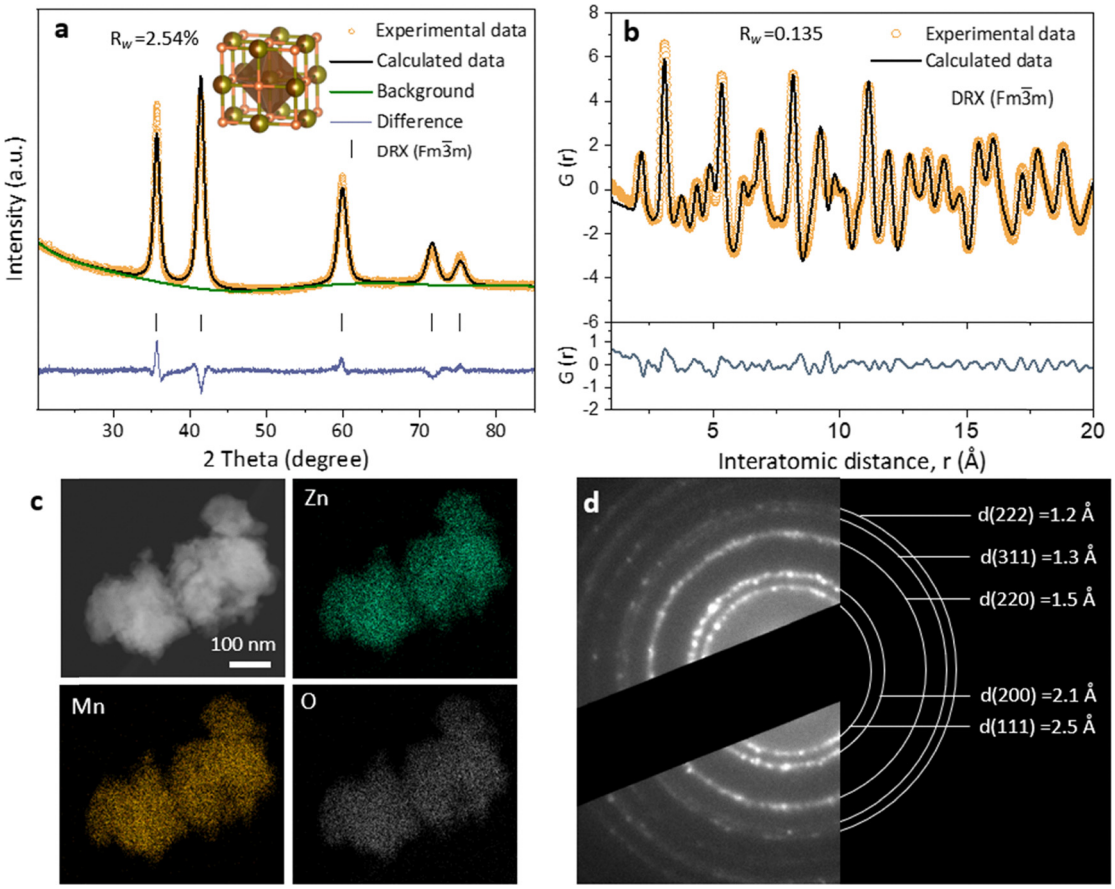

Fig. 1 Structural characterization of the DRX $ZnMnO_2$. (a) Powder XRD pattern of pristine cation-disordered $ZnMnO_2$, refined using the Rietveld method to the *Fm*$\bar{3}$m space group. (b) PDF analysis of pristine $ZnMnO_2$, derived from total X-ray scattering data collected at room temperature, and refined to the *Fm*$\bar{3}$*m* space group. (c) HAADF-STEM imaging and STEM-EDS mapping illustrating the elemental distribution of Zn, Mn, and O in pristine $ZnMnO_2$. (d) SAED pattern of $ZnMnO_2$ powder.

diffraction (SAED) pattern from many particles (Fig. 1d) reveals discrete diffraction rings, consistent with the XRD results and the expected reflections for $ZnMnO_2$.

Given the inherent instability of Mn(II)-based oxides, which are prone to dissolution in mildly acidic electrolytes,[31] this potential source of degradation to their electrochemical performance cannot be overlooked. To investigate this behaviour in DRX $ZnMnO_2$, we placed the material in a coin cell setup with electrolyte composed of 2 M $ZnSO_4$ and 0.2 M $MnSO_4$ additive, allowing it to rest. By "resting," we refer to a period during which the material is exposed to the electrolyte without any external bias being applied. During this resting period, we observed that $ZnMnO_2$ underwent a self-dissolution process. XRD analysis of the cathode material after various resting times in the aqueous electrolyte reveals that the intensity of peaks corresponding to the corrosion product zinc hydroxide sulphate ($(Zn(OH)_2)_3{\cdot}ZnSO_4{\cdot}nH_2O$, ZHS) increases over time (Fig. 2a). After resting for 1 hour, a peak at 12.4° corresponding to the (001) plane of $(Zn(OH)_2)_3{\cdot}ZnSO_4{\cdot}0.5H_2O$ (PDF#00-009-0204) is observed. As the resting time extends to 24 hours, an additional peak at 8.8° appears, assigned to the (001) plane of $(Zn(OH)_2)_3{\cdot}ZnSO_4{\cdot}4H_2O$ (PDF#00-044-0674). This evolution suggests that with prolonged resting, more water molecules are involved in the formation of hydrated ZHS phases. The self-dissolution process consumes H^+ ions, which increases the local pH and promotes ZHS formation. *In situ* pH measurements (Fig. S2) performed at the cathode surface reveal that the local pH gradually increases with prolonged resting time, eventually stabilizing after 6 hours. The proposed chemical reactions in this process are as follows:

$$H_2O \rightarrow H^+ + OH^-$$

$$ZnMnO_2 + 4H^+ \rightarrow Zn^{2+} + Mn^{2+} + 2H_2O$$

$$4Zn^{2+} + SO_4{}^{2-} + 6OH^- + nH_2O \rightarrow 3Zn(OH)_2{\cdot}ZnSO_4{\cdot}nH_2O$$

To verify this process, we conducted inductively coupled plasma optical emission spectroscopy (ICP-OES) analysis on the cathode material after different resting periods (Fig. 2b). The Mn/Zn molar ratio of the cathode increases with rest time, corroborating that dissolution of $ZnMnO_2$ occurs during rest accompanied by the formation of ZHS on the cathode. Further calculations were performed to quantify the amount of dissolved $ZnMnO_2$ (Fig. S3). It shows that the dissolution process is rapid; after just 1 h resting in electrolyte, 25.2 wt% of

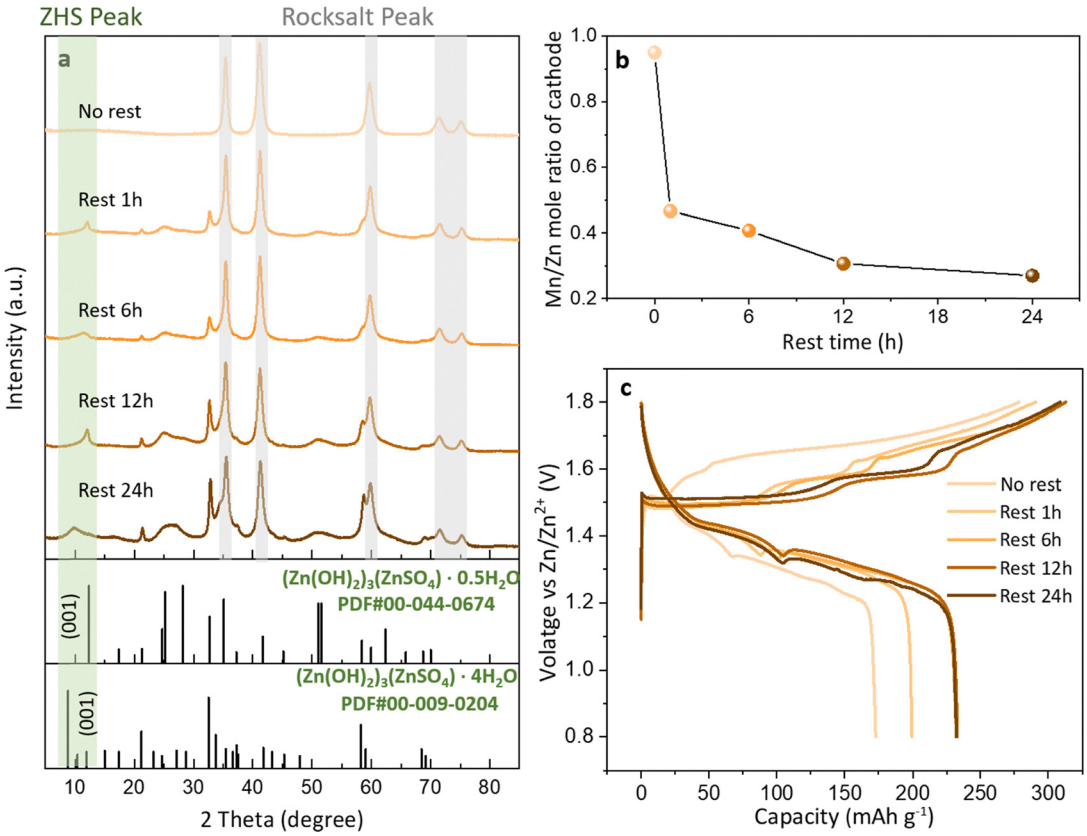

Fig. 2 Self-dissolution of DRX $ZnMnO_2$ during rest in aqueous electrolyte. (a) Powder XRD patterns of $ZnMnO_2$ after varying resting times in an electrolyte of 2 M $ZnSO_4$ with 0.2 M $MnSO_4$. The peak around 25° can be attributed to Super-P carbon. (b) ICP-OES analysis showing the Mn/Zn ratio of the $ZnMnO_2$ cathode after different resting periods in the same electrolyte. (c) The first charge/discharge curves of the $ZnMnO_2$ cathode paired with a Zn metal anode in 2 M $ZnSO_4$ with 0.2 M $MnSO_4$ at a current density of 10 mA g^{-1}, with different resting times prior to operation.

$ZnMnO_2$ is dissolved. The dissolution rate of $ZnMnO_2$ slows down after resting for 12 h, with 48.1 wt% dissolved. This deceleration is attributed to the gradual increase in local pH, which reaches equilibrium after prolonged resting, suppressing further dissolution. The complementing ICP-OES taken from the electrolyte shows the opposite Mn/Zn molar ratio change (Fig. S4), further supporting that cathode dissolution occurs during rest, and confirms that cathode dissolution significantly impacts the Mn and Zn concentration in the electrolyte (see supporting information discussion). Since part of the cathode material is entirely dissolved while the rest remains, this can be viewed as a purely chemical rather than an electrochemical reaction, with the valence state of Mn remaining unchanged.

X-ray absorption near edge spectroscopy (XANES) analysis (Fig. S5) confirms that the valence state of Mn does not evolve during resting. As a control, we tested the resting behaviour of $ZnMnO_2$ in deionized water and found no ZHS formed (Fig. S6a) and there was no valence change of Mn (Fig. S6b). This suggests that $ZnMnO_2$ does not undergo self-dissolution in neutral environments, with self-dissolution requiring the mildly acidic electrolyte.

This significant resting corrosion can be expected to have an influence on the cathode's properties. To investigate the effect of resting time on its electrochemical performance, we conducted tests on a full cell comprising a Zn metal anode and a $ZnMnO_2$ cathode in a 2 M $ZnSO_4$ electrolyte with 0.2 M $MnSO_4$ additive (Fig. 2c). The charge voltage profiles revealed differences based on resting time. The "No rest" condition exhibited a higher initial voltage. After a 1-hour resting period, the charging voltage profile displayed lower voltage with two distinct plateaus, a feature that persisted even after 24 hours of resting. The discharge capacity increased progressively with longer resting times, reaching its maximum value after 6 hours of resting. The observed changes in the charging voltage profile and the increase in discharge capacity with resting time can be attributed to two primary factors:

1. Mn^{2+} ion contribution: the increase in capacity can be attributed to the higher concentration of Mn^{2+} ions in the electrolyte resulting from cathode dissolution. During charging, it is expected that Mn^{2+} ions in the electrolyte are oxidized and redeposited on the cathode in the form of Mn-based oxide. To confirm the involvement of Mn^{2+}, a comparison experiment was conducted by placing $ZnMnO_2$ in a 2M $ZnSO_4$ electrolyte without the $MnSO_4$ additive and allowing it to rest for 12 hours (Fig. S7). The capacity in the electrolyte without the pre-added Mn was lower compared to the same resting time with the $MnSO_4$ additive, indicating that the presence of Mn^{2+} ions does contribute to capacity. This is consistent with previously

reported studies.[32,33] Therefore, as the resting time increases, more Mn^{2+} ions dissolve into the electrolyte, and participate in the charging process, leading to higher capacity.

2. Formation of ZHS: ZHS plays an important role in modulating the voltage profile during charging, as it can act as an OH^- reservoir to suppress pH fluctuations.[34,35] During charging, the process of oxidation of Mn^{2+} releases H^+ ions, leading to a decrease in pH. In response, ZHS dissolves and releases OH^- ions, effectively buffering pH. In a less acidic environment, the activation energy for Mn^{2+} to redeposit on the cathode as an Mn-based oxide is lower, facilitating more redeposition.[35–38] After resting in the electrolyte for 1 hour, ZHS begins to form on the cathode, lowering the oxidation voltage and promoting oxide redeposition, which leads to an increase in capacity. As the resting time increases, more ZHS is formed, further facilitating Mn oxide redeposition, which continues to improve the capacity until stabilizing after 6 h resting.

Since ZHS formation and cathode dissolution occur simultaneously, their individual contributions are difficult to decouple. For consistency, unless otherwise specified, all subsequent electrochemical performance tests and characterizations were conducted after a 12-hour resting period.

The electrochemical performance of the $ZnMnO_2$ cathode was further assessed (Fig. 3). The performance of anode-free cells using a carbon paper anode will be shown in Fig. 6.

Cyclic voltammetry (CV) was performed over the first five cycles to investigate the electrochemical redox behaviour of $ZnMnO_2$ (Fig. 3a). In the initial cycle, two anodic peaks appear at 1.55 V and 1.6 V (*vs.* Zn/Zn^{2+}), corresponding to the stepwise oxidation of Mn species. During subsequent cycles, both anodic peaks broaden, with the 1.55 V peak gradually decreasing in intensity and the 1.6 V peak shifting slightly to higher potential. This evolution suggests that structural change occurs during the initial cycles, which is confirmed by *ex situ* XRD presented later in Fig. 4.

The cathode's rate capability was tested at current densities of 10, 20, 100, and 250 mA g^{-1}. Galvanostatic charge/discharge curves are shown in Fig. 3b, corresponding to the first, fourth, seventh, and tenth cycles in Fig. 3c. At a current density of 10 mA g^{-1}, the charging capacity reaches 312.8 mAh g^{-1}. Some capacity is lost during discharging however, with the discharge capacity reaching 233 mAh g^{-1} at 10 mA g^{-1}. At a higher current density of 250 mA g^{-1}, the discharge capacity decreases further, to 99 mAh g^{-1}.

The extended cycling performance of $ZnMnO_2$ was evaluated at a current density of 20 mA g^{-1} and 100 mA g^{-1} (Fig. 3d and e). At both current densities, the capacity initially increases during the first few cycles, followed by a gradual decay. This "activation process" is related to gradual structural changes to spinel phase, which will be discussed later. Notably, cycling $ZnMnO_2$ at 100 mA g^{-1} demonstrated superior capacity retention over 250 cycles, in contrast to cycling at 20 mA g^{-1}, which showed reduced retention over 60 cycles.

The performance of our $ZnMnO_2$ is compared with other ZIB cathodes in Fig. 3f. The combination of good capacity and high discharge voltage gives $ZnMnO_2$ an energy density of 318.1 Wh kg^{-1} based on cathode mass, exceeding those of other zincated cathodes, including $ZnMn_2O_4$ (202 Wh kg^{-1}),[16] $Zn_{0.56}VOPO_4{\cdot}2H_2O$ (152.6 Wh kg^{-1}),[20] and $Zn_3[Fe(CN)_6]_2$ (100 Wh kg^{-1}).[22] Furthermore, its energy density even exceed

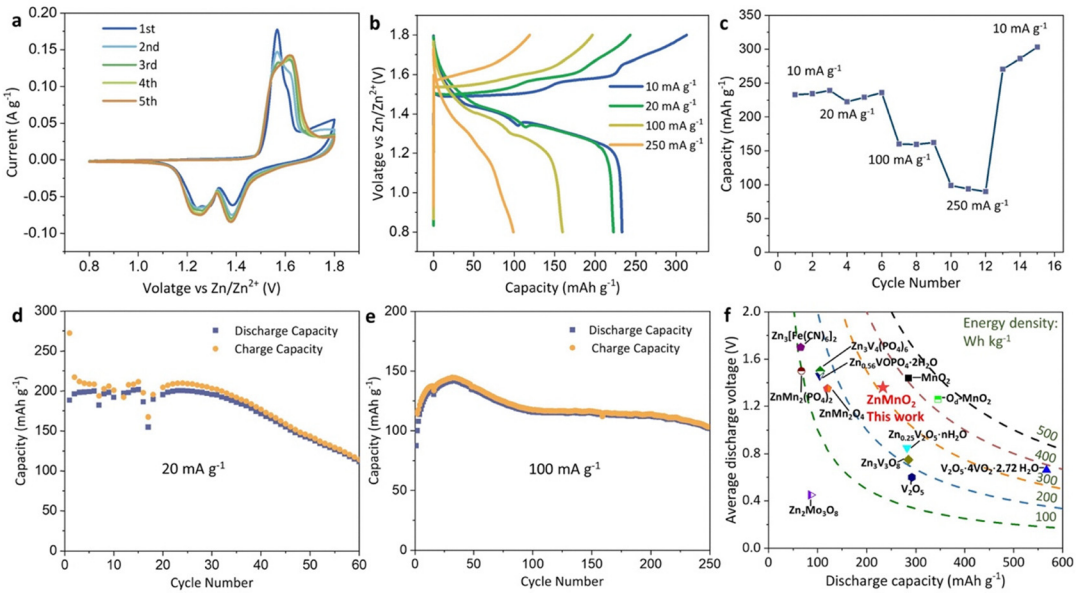

Fig. 3 Electrochemical performance of DRX $ZnMnO_2$. (a) CV of $ZnMnO_2$ at a scan rate of 0.05 mV s^{-1}. (b) The charge/discharge curves of $ZnMnO_2$ at various current densities within the voltage range of 0.8–1.8 V *vs.* Zn/Zn^{2+}. (c) Rate performance of discharge capacity of $ZnMnO_2$ at current densities of 10, 20, 100, and 250 mA g^{-1}. Cycling performance of $ZnMnO_2$ at (d) low current density (20 mA g^{-1}) and (e) high current density (100 mA g^{-1}). All cells utilized a $ZnMnO_2$ cathode paired with a Zn metal anode in an electrolyte of 2 M $ZnSO_4$ with 0.2 M $MnSO_4$. All cells were rested for 12 h before operation. (f) Comparison of average discharge voltage (*V*) *versus* discharge capacity (mAh g^{-1}) and energy density (Wh kg^{-1}) for various cathodes in ZIBs.[3,16,18,20–22,24,25,39–42]

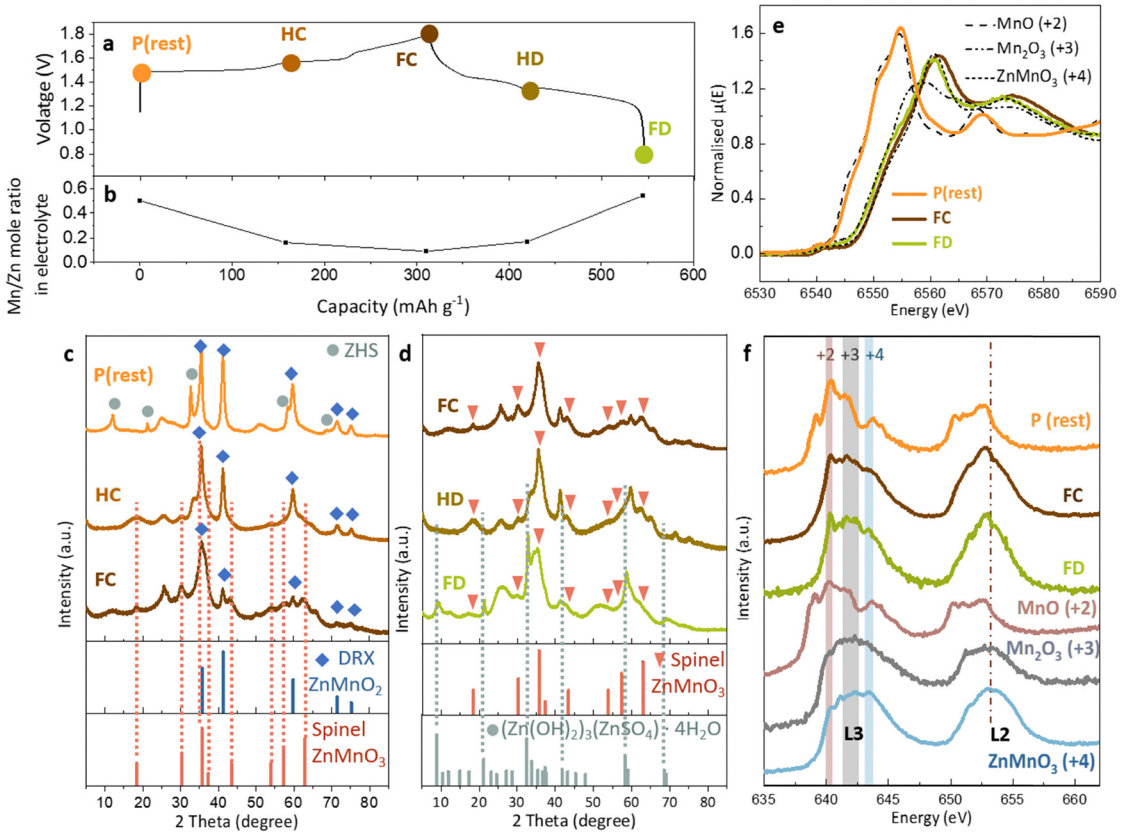

Fig. 4 The charge storage mechanism for DRX $ZnMnO_2$. (a) Initial charge/discharge curve of $ZnMnO_2$ at a current density of 10 mA g^{-1} in 2 M $ZnSO_4$ with 0.2 M $MnSO_4$ electrolyte. Coloured points highlight the states of charge chosen for *ex situ* XRD and spectroscopic analysis. (b) ICP-OES showing the Mn/Zn ratio in the electrolyte from the separators. (c) Powder XRD of the cathode at various charge states and (d) at various discharge states, with corresponding states marked in (a). The peak around 25° can be attributed to super-P carbon. (e) Mn K-edge XANES spectra of the cathode, and (f) Mn L-edge XAS spectra of the cathode collected in iPFY mode at various charge states, with corresponding states marked in (a). All cells were rested for 12 hours before operation. The labels in the figure are: P (rest) for the pristine state after resting in the electrolyte for 12 hours, HC for half charge, FC for full charge, HD for half discharge, and FD for full discharge.

some of the other more widely studied cathodes, such as $Zn_{0.25}V_2O_5{\cdot}nH_2O$ (250 Wh kg^{-1})[39] and V_2O_5 (175.2 Wh kg^{-1}),[3] although it is still lower than that of the main ZIB cathodes MnO_2 (410.4 Wh kg^{-1}),[40] O_d-MnO_2 (470 Wh kg^{-1}),[41] and $V_2O_5{\cdot}4VO_2{\cdot}2.72H_2O$ (375 Wh kg^{-1}).[42] The comparison shows that the advantages of $ZnMnO_2$, in offering a well-balanced combination of good capacity, high discharge voltage, and competitive energy density while also being natively zinc containing, position it as a promising cathode material for anode-free aqueous ZIBs.

The energy storage mechanism of the DRX $ZnMnO_2$ cathode was investigated by analyzing its structural and valence changes. Structural changes were determined using *ex situ* powder XRD (Fig. 4c and d). At the pristine stage, after resting in the electrolyte for 12 hours, the cathode contained the original DRX material plus additional formed ZHS due to cathode dissolution during resting, as discussed earlier alongside Fig. 2. As the cell reached a half-charge state, the intensity of the ZHS-related peaks decreased. By the time the cell was fully charged, the ZHS peaks had disappeared entirely, indicating that ZHS dissolved during charging. Since no electron transfer occurs during the ZHS dissolution process, ZHS itself does not contribute to the overall capacity during charging.

Interestingly, at full charge, the DRX cathode partially transformed into a spinel phase, with 90.8 wt% spinel and 9.2 wt% rocksalt remaining, as determined by XRD refinement (Fig. S8 and Table S2). Based on refinement of the XRD pattern, the composition of the spinel phase is determined to be $Zn_{0.79}Mn_{1.11}O_3$, as shown in Table S2. Given its non-stoichiometric nature, this phase is referred to as $Zn_xMn_yO_3$. ICP-OES analysis of the cathode at different charge states (Fig. S9) support the top of charge structure refinement findings, with detailed discussion presented in the supporting information. XRD of the discharged sample (Fig. 4d) shows the spinel phase remained stable throughout the discharge process and did not revert to the original rocksalt structure, indicating that this phase transformation from rocksalt to spinel is irreversible. The XRD also shows that ZHS reformed at discharge due to local pH changes.

To further elucidate the redox mechanism, we compared lattice changes related with Zn deintercalation/intercalation with XRD data. Focusing on the (200) plane around 41° and the (311) and (222) planes near 72°–75° for the DRX phase, we monitored unit cell changes related to Zn^{2+} movement (see Fig. S10). The negligible change in the unit cell during charging and discharging indicates that Zn^{2+} cannot be effectively

deintercalated from the DRX structure, likely due to limited zinc-ion diffusion possible in the close-packed face-centered cubic lattice.[43] In contrast, the *in situ*-formed spinel phase enables reversible Zn^{2+} intercalation and deintercalation. This is evidenced by spinel phase peaks at the (220) plane around 30° and the (440) plane around 63° during the first discharge (Fig. S11) and the second cycle (Fig. S12c), which exhibit subtle peak shifts indicative of unit cell contraction and expansion associated with Zn^{2+} deintercalation/intercalation.

The irreversible phase transition from DRX to a spinel phase reveals a parallel between Zn- and Li-based DRX materials. In Li-ion batteries, Mn-rich DRX cathodes undergo an *in situ* transformation to a spinel-like ordering during cycling, named as the ''δ-phase'' by the Ceder group.[44,45] This transformation is accelerated by higher Mn content due to the enhanced mobility of Mn,[45] and further studies confirm that the transition is both thermodynamically favourable and kinetically accessible, but only happens in the delithiated DRX state.[46] In contrast, Zn-based DRX $ZnMnO_2$ shows a divergence: Zn^{2+} remains trapped in the structure because it cannot deintercalate, leaving no vacancies for Mn migration. This raises the question as to nature of the driving force behind the transition from DRX $ZnMnO_2$ to $Zn_xMn_yO_3$ spinel, which needs further research. Notably, a similar phenomenon has been observed in MnS rocksalt cathodes in aqueous ZIBs, where a transition to $ZnMnO_3$ spinel occurs during charging,[47] suggesting that a different mechanism may exist in aqueous ZIB systems.

To understand the redox behaviour of Mn, Mn K-edge XANES measurements were conducted for pristine after 12 h rest (P(rest)), fully charged (FC), and fully discharged (FD) states of charge of the $ZnMnO_2$ cathode (Fig. 4e). Linear combination fitting (LCF) was used to estimate the valence state of Mn in the electrode. Initially, the Mn valence was 2.04. After the first charge, it increased to 3.72, corresponding to a transfer of 1.68 electrons per metal centre. However, after discharge, the Mn valence only reduced to 3.55 and did not return to its initial state. Complementary soft XAS experiments were conducted to characterize the Mn L-edge using inverse partial fluorescence yield (iPFY) mode, which effectively mitigates Mn self-absorption artifacts. The crystal field splitting in the L_3 region allows the discrimination of multiplet features,[48] where the peaks at 640.3 eV, 642 eV, and 643.5 eV are assigned to Mn^{2+}, Mn^{3+} and Mn^{4+}, respectively, in good agreement with previously reported studies.[48,49] The spectra confirmed Mn^{2+} existence in the pristine state and the Mn^{2+}/Mn^{4+} redox couple is involved during charging. Notably, even at the top of charge, Mn^{2+} signals remain, which is evidenced by comparison of the iPFY XAS spectrum of the fully charged cathode with reference spectra (Fig. S13). This is consistent with XRD results showing that a small fraction of DRX persists, retaining Mn^{2+}. During discharge, the Mn valence exhibits only a slight decrease, which is insufficient to fully account for the delivered capacity. Combining the results from XRD, XANES and iPFY measurements, we can be confident that while reversible Zn intercalation/deintercalation in the spinel phase contributes to energy storage, an additional mechanism must be responsible for the majority of the capacity.

One possible route involves the oxidation of Mn^{2+} to Mn^{4+} during charging and the reduction of Mn^{4+} to Mn^{2+} during discharging, accompanied by its dissolution into the electrolyte. To investigate this, the electrolyte in the separator was analysed using ICP-OES (Fig. 4b). The initial Mn/Zn molar ratio, prior to cycling but after the cell having rested for 12 hours, was 0.49, compared to 0.1 in the non-resting state (Fig. S4), due to the dissolution of $ZnMnO_2$ into the electrolyte. The Mn/Zn ratio during the charging process decreased as $ZnMnO_2$ reacted with Mn^{2+} and water to form the $Zn_xMn_yO_3$ spinel. However, during discharge, Mn^{2+} dissolved back into the electrolyte, causing the Mn/Zn ratio to return to a value similar to that of the pristine state. This reversible change in the Mn/Zn ratio of electrolyte during charging and discharging indicates that this dissolution and deposition process dominates energy storage. ICP-OES analysis of the electrolyte at second cycle (Fig. S12a) showed a similar reversible pattern, with the Mn/Zn ratio decreasing during charging and increasing during discharging, further confirming that the majority of capacity is derived from this dissolution and (re-)deposition mechanism. The proposed reaction formula for this process is as follows:

First charge:

$$H_2O + (y-1)\,Mn^{2+} + ZnMnO_2 - (6-2x-2y)e^- \rightarrow Zn_xMn_yO_3 + 2H^+ + (1-x)\,Zn^{2+}$$

$$3Zn(OH)_2{\cdot}ZnSO_4{\cdot}nH_2O \rightarrow 4Zn^{2+} + {SO_4}^{2-} + 6OH^- + nH_2O$$

First discharge and following cycle:

$$Zn_xMn_yO_3 + 6H^+ + (6-2x-2y)e^- \rightleftharpoons 3H_2O + yMn^{2+} + xZn^{2+}$$

$$4Zn^{2+} + {SO_4}^{2-} + 6OH^- + nH_2O \rightleftharpoons 3Zn(OH)_2{\cdot}ZnSO_4{\cdot}nH_2O$$

XRD analysis of the second cycle, including charging and discharging (Fig. S12c), reveals that the electrode retains its spinel structure, confirming that the phase transition from disordered rocksalt to spinel at first charge is irreversible. With further cycling, the remaining DRX phase gradually decreases and eventually transforms completely into the spinel phase. Further XRD Rietveld refinement after 15 cycles after full charge (Fig. S14 and Table S3) shows peaks only corresponding to $Zn_xMn_yO_3$, with no remaining rocksalt phase. This gradual transformation from rocksalt to spinel during repeated cycling suggests that the spinel phase eventually becomes the dominant structure. The cumulative transformation into the spinel phase during cycling likely contributes to the observed capacity increase in the initial cycles, as it enables greater Zn^{2+} intercalation/deintercalation (Fig. 3d and e). Additionally, this phase transition may account for the gradual peak shifts observed in the CV curves (Fig. 3a). The relative phase fractions of $Zn_xMn_yO_3$ and ZHS after 15 cycles at full discharge are calculated and discussed in Fig. S15.

We summarize the proposed storage mechanism of $ZnMnO_2$ DRX cathode in Fig. 5. When the cathode is resting in a mildly acidic electrolyte, the $ZnMnO_2$ will partially dissolve and ZHS will be formed as the local pH increases due to proton

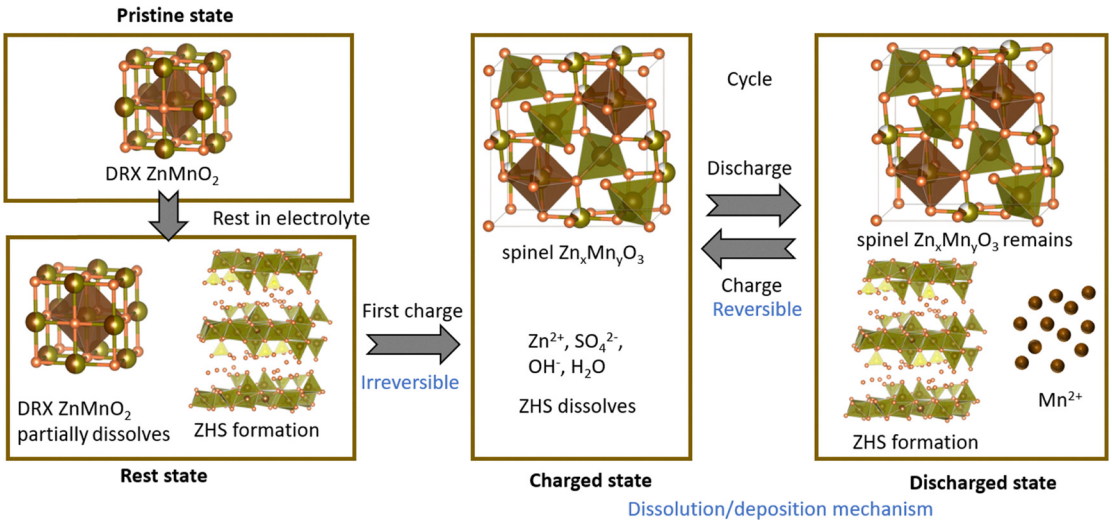

Fig. 5 Schematic of the energy storage mechanism for the $ZnMnO_2$ DRX cathode in an aqueous ZIB.

consumption. During the first charge, the DRX $ZnMnO_2$ undergoes an irreversible phase transition to a $Zn_xMn_yO_3$ spinel structure, while the ZHS dissolves. In subsequent cycles, the spinel phase becomes the dominant cathode material, unlocking the ability to store charge *via* Zn^{2+} intercalation/deintercalation, but mainly storing energy through the dissolution and deposition of Mn.

To further explore the potential of Zn-containing cathodes, their performance in anode-free (*i.e.*, no Zn metal) configurations was investigated. In a standard ZIB (Fig. 6a), the Zn anode reacts with the aqueous electrolyte over time, leading to capacity loss and a deterioration of its shelf life. In our full-cells the Zn anode thickness reaches up to 180 μm, which corresponds to a high N/P ratio of 50 for a Zn/$ZnMnO_2$ cell—a commonly reported value in several studies.[7,8,50,51] By contrast, the anode-free ZIB (Fig. 6a) reduces the N/P ratio to effectively zero by eliminating the Zn metal anode. The lack of Zn metal on the initial anode prevents the hydrogen evolution reaction and Zn corrosion when the cell is idle, which would contribute to improved cell shelf life.

In this study, we used the standard ZIB electrolyte of 2 M $ZnSO_4$ with 0.2 M $MnSO_4$, which is cheap and safe. The only modification of our anode-free cell was the replacement of the Zn metal anode with a carbon paper current collector. The charging/discharging profile of the anode-free ZIB (Fig. 6b) is compared with that of a standard ZIB in Fig. S16. The two profiles exhibit similar features, indicating comparable redox processes, but the anode-free cell shows greater polarization. Across repeated cycling, the anode-free ZIB showed good capacity retention at 100 mA g^{-1} over 100 cycles and a coulombic efficiency exceeding 91.16% after the second cycle (Fig. 6c). However, compared to the performance of the cell using a Zn foil anode (Fig. S17), there is significant degradation. This performance decay is not surprising, as the anode-free cell lacks the deep Zn reservoir of a metal anode, meaning any Zn lost due to side reactions or irreversible plating/stripping is unable to be replaced.

Despite the reduction in capacity, eliminating the Zn metal anode comes with the benefit of significantly enhancing the energy density of the full cell. Studies often calculate battery energy density based solely on the mass of the active cathode material, often overlooking the impact of the anode. In this work, the energy density based on the mass of the active material can reach 214.9 Wh kg^{-1} at current densities of 100 mA g^{-1}. However, when the mass of the metallic Zn anode and the entire cathode (including active material, carbon, and binder) is considered, the energy density at 100 mA g^{-1} drops drastically to 3.1 Wh kg^{-1} due to the heavy Zn metal, which weighs 332 mg (16 mm in diameter with thickness of 180 μm). By contrast, using carbon paper as the anode, which weighs just 10 mg for the same size (16 mm in diameter with thickness of 100 μm), the energy density based on the anode and the entire cathode reaches 20.9 Wh kg^{-1}—nearly 7 times higher than cell with a Zn metal anode, despite the lower capacity. A detailed calculation is provided in the supporting information with additional discussion.

As shown in Fig. S17, the $ZnMnO_2$ cathode paired with carbon paper exhibits lower capacity and poorer capacity retention compared to when it is paired with a Zn anode. While the anode-free configuration offers advantages, such as improved shelf life by removing the metal source of aging side-reactions during cell storage (Fig. S18), and offering a higher energy density by replacing metal Zn with just a lightweight current collector, several challenges remain. During operation, Zn is still reversibly deposited and stripped on the current collector, which introduces practical issues. These include incomplete utilization of deposited Zn, leading to the formation of electrochemically inactive 'dead Zn', low stripping/plating efficiency, and electrolyte depletion over extended cycling. Furthermore, dendritic Zn growth, an unstable Zn–electrolyte interface, and parasitic side reactions continue to compromise both cycling stability and coulombic efficiency. These issues lead to more rapid performance decay in an anode-free configuration than would be seen in a conventional ZIB, as the anode-free cell

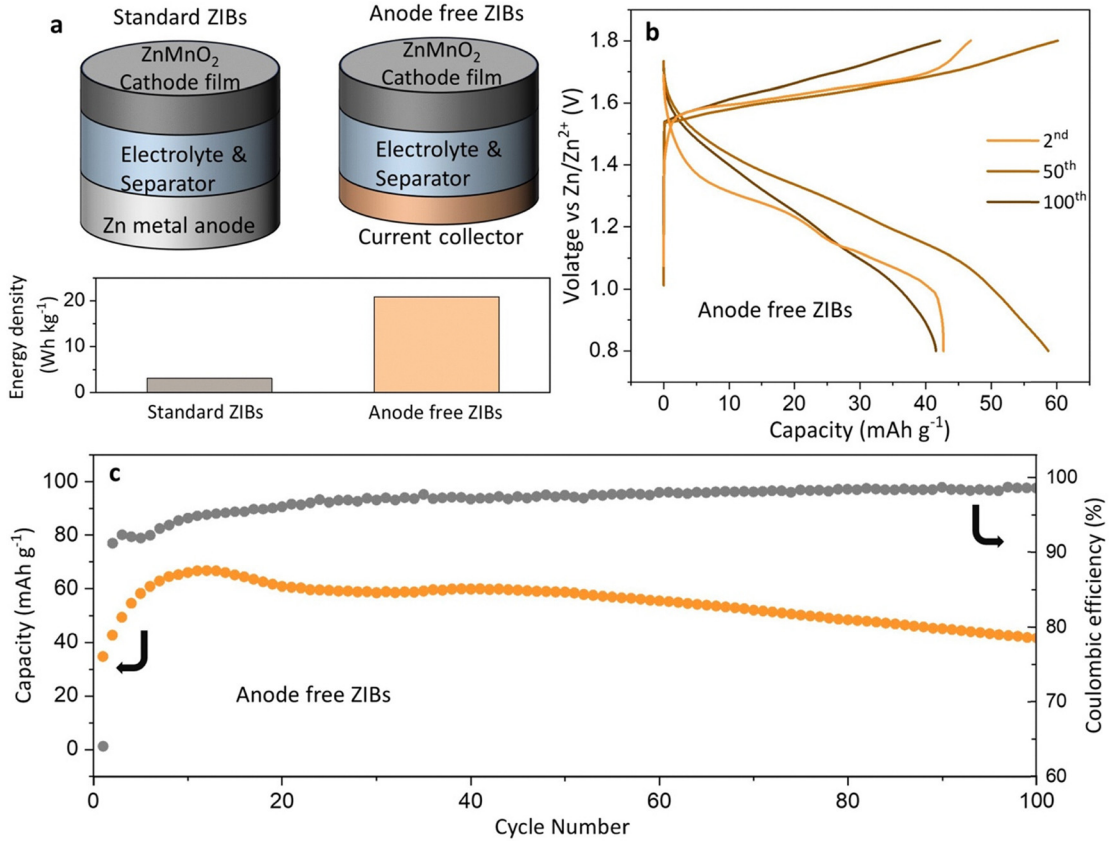

Fig. 6 Employing a DRX $ZnMnO_2$ cathode in an anode-free aqueous ZIB. (a) Schematic of standard and anode-free ZIB using $ZnMnO_2$ DRX cathode and their energy density based on the total mass of both cathode and anode. (b) The charging/discharging curve of $ZnMnO_2$ based anode-free ZIB with carbon paper as the current collector at 100 mA g^{-1}. (c) Cycling performance of $ZnMnO_2$ based anode-free ZIB at 100 mA g^{-1}, showing the discharge capacity and coulombic efficiency. All cells were rested for 12 h before operation.

lacks a reservoir of replacement active Zn material to draw upon, an attribute that would be provided for by the metal anode in a conventional ZIB.

These issues may be mitigated through electrolyte engineering or by developing high-capacity intercalation-type anodes. Alternative Zn metal-free anodes, such as TiS_2,[52] have been explored to create rocking-chair Zn-ion batteries (Fig. S19), which can ideally avoid the problems associated with irreversible Zn plating and stripping. However, it still shows inferior performance compared to cells using Zn metal. For anode-free cells to be a viable consideration against conventional ZIBs, additional research will be needed to develop better electrolytes and alternative current collectors or anode host materials.

To gain further insight into the origin of performance limitations in anode-free Zn cells, we systematically investigated whether the performance-limiting factor arises from the cathode or the anode. We synthesized seven other natively Zn-containing cathode materials that are compatible with anode-free cell configurations. Fig. S20–S27 show the performance of both Zn metal cells and anode-free cells paired with these seven candidate cathodes: $ZnMn_2O_4$, $Zn_3V_3O_8$, $Zn_3V_4(PO_4)_6$, $Zn_3[Fe(CN)_6]_2$, $ZnMn_2(PO_4)_2$, $Zn_2Mo_3O_8$, and $Zn_{0.56}VOPO_4{\cdot}2H_2O$ as a comparison to our newly developed DRX $ZnMnO_2$ cathodes, all cycled in the same electrolyte (2 M $ZnSO_4$ with no Mn additive) and at the same current density of 100 mA g^{-1}.

The electrochemical performance of these materials was evaluated in both standard ZIBs using Zn foil anodes and anode-free ZIBs using a carbon paper current collector at the anode. In every case, the capacity and cycling performance of the anode-free cells was worse than that of the corresponding Zn metal cells. Since these cathodes encompass a wide range of transition metals, compositions, and structural types, their consistently inferior performance in the anode-free configuration indicates that the limiting factor is primarily associated with the anode side, specifically the reversibility of Zn plating and stripping, rather than the cathode.

These studies show that realizing the potential advantages of an anode-free ZIB, where removing the Zn metal would yield both higher energy density and negate the source of open-circuit aging side reactions, remains highly challenging beyond just the development of new zincated cathodes. Significant developments in current collector and anode host materials, along with appropriately tailored electrolytes, will also be required if an anode-free approach is to be a realistic alternative to using a high N : P ratio metal anode.

As part of our exploration of this first synthesis and application of Zn-containing DRX for aqueous ZIBs, we have also

demonstrated that other transition metal-based DRX oxides can be synthesized and utilized. We prepared $ZnFeO_2$ as an alternative DRX cathode material and found that it, too, exhibits first-charge capability (Fig. S28). Being able to workably utilize Fe, an earth-abundant and cost-effective element, in place of Mn shows the potentially versatility of our synthesis approach, paving the way for a broader range of DRX materials with tuneable properties.

Conclusion

The development of a novel $ZnMnO_2$ cathode for the aqueous ZIB addresses the lack of high-capacity, high discharge voltage Zn-containing cathodes suitable for anode-free cells. The $ZnMnO_2$ material, with a cation-disordered rocksalt structure, exhibits a high discharge capacity of 233 mAh g^{-1} and demonstrates stable cycling performance. Notably, the $ZnMnO_2$ cathode is capable of initial charging, making it suitable for anode-free ZIB designs. By replacing the zinc metal anode with carbon paper as the current collector, the energy density of the cell is significantly enhanced—nearly seven times higher than cell with Zn metal anode, despite a lower capacity. The energy storage mechanism of this novel $ZnMnO_2$ cathode was elucidated through various characterization techniques, revealing that a Zn intercalation/deintercalation contribution arises due to an irreversible shift from a disordered rocksalt structure to spinel, however its capacity remains primarily governed by the dissolution and deposition of Mn. This work highlights the potential of anode-free ZIB designs to achieve higher energy densities, albeit with significant remaining challenges. The study also shows the potential of DRX oxides based on earth abundant transition metals, including $ZnMnO_2$ and $ZnFeO_2$, as efficient cathode materials, contributing to the ongoing development of sustainable and high-performance cathodes for aqueous ZIBs.

Conflicts of interest

There are no conflicts to declare.

Data availability

All data is available upon reasonable request from the corresponding authors.

Supplementary information is available. See DOI: **https://doi.org/10.1039/d5ee02643a**.

Acknowledgements

AWR thanks the Royal Society (URF\R\221018) and the EPSRC (EP/Z000483/1). AM and LFJP acknowledge support from HMV Catapult at WMG. The authors acknowledge financial support provided by the Henry Royce Institute (grant ref EP/R010145/1), and the Henry Royce Institute for Advanced Materials (EP/R00661X/1, EP/S019367/1 and EP/R010145/1). Beamline BM28 of the ESRF, XMaS, is a UK national research facility supported by EPSRC (EP/Y031962/1), and we are grateful to the beamline staff for their support. We acknowledge Diamond Light Source for time on beamline I15 and are grateful to the beamline staff for their support. We acknowledge BL27SU in SPring-8, RIKEN, and are grateful to the beamline staff for their support. The authors gratefully acknowledge; the Warwick Physics and Chemistry Workshop Facility (Lance Fawcett, Daisy Ashworth, Matty Mills, Jeanette Weston); the David Cockayne Centre for Electron Microscopy at the University of Oxford for their access and support (Phani Karamched, Graham Wyatt, Neil Young, Gareth Hughes); the Electron Microscopy RTP at the University of Warwick for their access and support (Andrew Unsworth, Steve York, Yisong Han, Steve Hindmarsh); the X-Ray Diffraction RTP at the University of Warwick for their access and support (David Walker, Jie Liu); and Trang To in the School of Geography and the Environment at the University of Oxford's Geolabs for performing ICP-MS measurements.

References

1 Y. Fu, Q. Wei, G. Zhang, X. Wang, J. Zhang, Y. Hu, D. Wang, L. Zuin, T. Zhou, Y. Wu and S. Sun, High-performance reversible aqueous Zn-ion battery based on porous MnO_x nanorods coated by MOF-derived N-doped carbon, *Adv. Energy Mater.*, 2018, **8**(26), 1801445, DOI: **10.1002/aenm.201801445**.

2 M. H. Alfaruqi, V. Mathew, J. Gim, S. Kim, J. Song, J. P. Baboo, S. H. Choi and J. Kim, Electrochemically induced structural transformation in a γ-MnO_2 cathode of a high capacity zinc-ion battery system, *Chem. Mater.*, 2015, **27**(10), 3609–3620, DOI: **10.1021/cm504717p**.

3 P. Hu, M. Yan, T. Zhu, X. Wang, X. Wei, J. Li, L. Zhou, Z. Li, L. Chen and L. Mai, Zn/V_2O_5 aqueous hybrid-ion battery with high voltage platform and long cycle life, *ACS Appl. Mater. Interfaces*, 2017, **9**(49), 42717–42722, DOI: **10.1021/acsami.7b13110**.

4 X. Chen, L. Wang, H. Li, F. Cheng and J. Chen, Porous V_2O_5 nanofibers as cathode materials for rechargeable aqueous zinc-ion batteries, *J. Energy Chem.*, 2019, **38**, 20–25.

5 Z. Li and A. W. Robertson, Electrolyte engineering strategies for regulation of the Zn metal anode in aqueous Zn-ion batteries, *Battery Energy*, 2023, **2**(1), 20220029, DOI: **10.1002/bte2.20220029**.

6 S. D. Pu, B. Hu, Z. Li, Y. Yuan, C. Gong, Z. Ning, C. Chau, S. Yang, S. Zhang, L. Pi, Y. T. Tang, J. Yue, T. J. Marrow, X. Gao, P. G. Bruce and A. W. Robertson, Decoupling, quantifying, and restoring aging-induced Zn-anode losses in rechargeable aqueous zinc batteries, *Joule*, 2023, **7**(2), 366–379.

7 G. Zampardi and F. La Mantia, Open challenges and good experimental practices in the research field of aqueous Zn-ion batteries, *Nat. Commun.*, 2022, **13**(1), 687.

8 J. Zheng, Q. Zhao, T. Tang, J. Yin, C. D. Quilty, G. D. Renderos, X. Liu, Y. Deng, L. Wang, D. C. Bock,

C. Jaye, D. Zhang, E. S. Takeuchi, K. J. Takeuchi, A. C. Marschilok and L. A. Archer, Reversible epitaxial electrodeposition of metals in battery anodes, *Science*, 2019, **366**(6465), 645–648, DOI: 10.1126/science.aax6873.

9 P. He and J. Huang, Chemical passivation stabilizes Zn anode, *Adv. Mater.*, 2022, **34**(18), 2109872, DOI: 10.1002/adma.202109872.

10 C. Deng, X. Xie, J. Han, Y. Tang, J. Gao, C. Liu, X. Shi, J. Zhou and S. Liang, A sieve-functional and uniform-porous kaolin layer toward stable zinc metal anode, *Adv. Funct. Mater.*, 2020, **30**(21), 2000599, DOI: 10.1002/adfm.202000599.

11 X. Zhao, X. Zhang, N. Dong, M. Yan, F. Zhang, K. Mochizuki and H. Pan, Advanced buffering acidic aqueous electrolytes for ultra-long life aqueous zinc-ion batteries, *Small*, 2022, **18**(21), 2200742, DOI: 10.1002/smll.202200742.

12 X. Zeng, J. Mao, J. Hao, J. Liu, S. Liu, Z. Wang, Y. Wang, S. Zhang, T. Zheng, J. Liu, P. Rao and Z. Guo, Electrolyte design for *in situ* construction of highly Zn^{2+}-conductive solid electrolyte interphase to enable high-performance aqueous Zn-ion batteries under practical conditions, *Adv. Mater.*, 2021, **33**(11), 2007416, DOI: 10.1002/adma.202007416.

13 Y. Bai, H. Zhang, W. Liang, C. Zhu, L. Yan and C. Li, Advances of Zn metal-free ''Rocking-Chair''-type zinc ion batteries: recent developments and future perspectives, *Small*, 2024, **20**(8), 2306111, DOI: 10.1002/smll.202306111.

14 F. Ming, Y. Zhu, G. Huang, A. H. Emwas, H. Liang, Y. Cui and H. N. Alshareef, Co-solvent electrolyte engineering for stable anode-free zinc metal batteries, *J. Am. Chem. Soc.*, 2022, **144**(16), 7160–7170, DOI: 10.1021/jacs.1c12764.

15 S. Xie, Y. Li and L. Dong, Stable anode-free zinc-ion batteries enabled by alloy network-modulated zinc deposition interface, *J. Energy Chem.*, 2023, **76**, 32–40.

16 N. Zhang, F. Cheng, Y. Liu, Q. Zhao, K. Lei, C. Chen, X. Liu and J. Chen, Cation-Deficient Spinel $ZnMn_2O_4$ Cathode in $Zn(CF_3SO_3)_2$ Electrolyte for Rechargeable Aqueous Zn-Ion Battery, *J. Am. Chem. Soc.*, 2016, **138**(39), 12894–12901, DOI: 10.1021/jacs.6b05958.

17 J. C. Knight, S. Therese and A. Manthiram, Chemical extraction of Zn from $ZnMn_2O_4$-based spinels, *J. Mater. Chem. A*, 2015, **3**(42), 21077–21082.

18 J. Wu, Q. Kuang, K. Zhang, J. Feng, C. Huang, J. Li, Q. Fan, Y. Dong and Y. Zhao, Spinel $Zn_3V_3O_8$: a high-capacity zinc supplied cathode for aqueous Zn-ion batteries, *Energy Storage Mater*, 2021, **41**, 297–309.

19 R. Sun, P. Xia, X. Guo, S. Dong, F. Xu, Y. Zhang, S. Lu, Q. Zheng and H. Fan, Ternary $Zn_3V_3O_8$ superstructure and synergistic modification of separator promote high performance and stable zinc ion battery, *Chem. Eng. J.*, 2024, **486**, 150377.

20 D. Zhao, X. Pu, C. Wang, Z. Pan, M. Ding, Y. Cao and Z. Chen, Low-strain layered $Zn_{0.56}VOPO_4{\cdot}2H_2O$ as a high-voltage and long-lifespan cathode material for Zn-ion batteries, *Energy Storage Mater*, 2024, **66**, 103239.

21 D. Zhao, S. Chen, Y. Lai, M. Ding, Y. Cao and Z. Chen, A stable rocking-chair zinc-ion battery boosted by low-strain $Zn_3V_4(PO_4)_6$ cathode, *Nano Energy*, 2022, **100**, 107520.

22 L. Zhang, L. Chen, X. Zhou and Z. Liu, Towards high-voltage aqueous metal-ion batteries beyond 1.5 V: The zinc/zinc hexacyanoferrate system, *Adv. Energy Mater.*, 2015, **5**(2), 1400930, DOI: 10.1002/aenm.201400930.

23 Z. Pan, G. Ni, Y. Li, Y. Shi, F. Zhu, P. Cui and C. Zhou, Stabilizing Zinc Hexacyanoferrate Cathode by Low Contents of Cs Cations for Aqueous Zn-Ion Batteries, *ChemSusChem*, 2024, **17**(21), e202400713, DOI: 10.1002/cssc.202400713.

24 L. F. Zhou, X. W. Gao, T. Du, H. Gong, L. Y. Liu and W. B. Luo, A new phosphate member: $ZnMn_2(PO_4)_2$ as an advanced cathode material for aqueous and nonaqueous zinc ion batteries, *J. Alloys Compd.*, 2022, **905**, 163939.

25 K. Zhang, Q. Kuang, J. Wu, N. Wen, Q. Fan, Y. Dong and Y. Zhao, Layered structural $Zn_2Mo_3O_8$ as electrode material for aqueous zinc-ion batteries, *Electrochim. Acta*, 2022, **403**, 139629.

26 R. J. Clément, Z. Lun and G. Ceder, Cation-disordered rocksalt transition metal oxides and oxyfluorides for high energy lithium-ion cathodes, *Energy Environ. Sci.*, 2020, **13**(2), 345–373.

27 J. Lee, A. Urban, X. Li, D. Su, G. Hautier and G. Ceder, Unlocking the potential of cation-disordered oxides for rechargeable lithium batteries, *Science*, 2014, **343**(6170), 519–522, DOI: 10.1126/science.1246432.

28 A. N. Baranov, P. S. Sokolov and V. L. Solozhenko, ZnO under pressure: From nanoparticles to single crystals, *Crystals*, 2022, **12**(5), 744.

29 S. F. Dubinin, V. I. Maksimov, V. D. Parkhomenko, V. I. Sokolov, A. N. Baranov, P. S. Sokolov and Y. A. Dorofeev, Fine structure and magnetism of the cubic oxide compound $Ni_{0.3}Zn_{0.7}O$, *Phys. Solid State*, 2011, **53**(7), 1362–1366, DOI: 10.1134/S1063783411070092.

30 L. L. Driscoll, E. H. Driscoll, B. Dong, F. N. Sayed, J. N. Wilson, C. A. O'Keefe, D. J. Gardner, C. P. Grey, P. K. Allan, A. A. Michalchuk and P. R. Slater, Under pressure: offering fundamental insight into structural changes on ball milling battery materials, *Energy Environ. Sci.*, 2023, **16**(11), 5196–5209.

31 Y. Liu, Y. Ma, W. Yang, S. Bao, H. Chen and M. Xu, Spontaneously dissolved MnO: A better cathode material for rechargeable aqueous zinc-manganese batteries, *Chem. Eng. J.*, 2023, **473**, 145490.

32 C. Qiu, X. Zhu, L. Xue, M. Ni, Y. Zhao, B. Liu and H. Xia, The function of Mn^{2+} additive in aqueous electrolyte for Zn/δ-MnO_2 battery, *Electrochim. Acta.*, 2020, **351**, 136445.

33 V. Soundharrajan, B. Sambandam, S. Kim, S. Islam, J. Jo, S. Kim, V. Mathew, Y. K. Sun and J. Kim, The dominant role of Mn^{2+} additive on the electrochemical reaction in $ZnMn_2O_4$ cathode for aqueous zinc-ion batteries, *Energy Storage Mater.*, 2020, **28**, 407–417.

34 L. Godeffroy, I. Aguilar, J. Médard, D. Larcher, J. M. Tarascon and F. Kanoufi, Decoupling the dynamics of zinc hydroxide sulfate precipitation/dissolution in aqueous Zn–MnO_2 batteries by operando optical microscopy: a missing piece of the mechanistic puzzle, *Adv. Energy Mater.*, 2022, **12**(30), 2200722, DOI: 10.1002/aenm.202200722.

35 K. H. Ha, H. Moon, E. J. Joo, D. H. Jo and K. T. Lee, Role of zinc hydroxysulfates in the thermodynamics and kinetics of mild-acid Zn-MnO_2 batteries, *Energy Storage Mater*, 2024, **65**, 103150.

36 O. Fitz, C. Bischoff, M. Bauer, H. Gentischer, K. P. Birke, H. M. Henning and D. Biro, Electrolyte study with in operando pH tracking providing insight into the reaction mechanism of aqueous acidic Zn//MnO_2 batteries, *ChemElectroChem*, 2021, **8**(18), 3553–3566, DOI: **10.1002/celc.202100888**.

37 H. Chen, C. Dai, F. Xiao, Q. Yang, S. Cai, M. Xu, H. J. Fan and S. J. Bao, Reunderstanding the reaction mechanism of aqueous Zn–Mn batteries with sulfate electrolytes: role of the zinc sulfate hydroxide, *Adv. Mater.*, 2022, **34**(15), 2109092, DOI: **10.1002/adma.202109092**.

38 I. Aguilar, P. Lemaire, N. Ayouni, E. Bendadesse, A. V. Morozov, O. Sel, V. Balland, B. Limoges, A. M. Abakumov, E. Raymundo-Piñero, A. Slodczyk, A. Canizarès, D. Larcher and J. M. Tarascon, Identifying interfacial mechanisms limitations within aqueous Zn-MnO_2 batteries and means to cure them with additives, *Energy Storage Mater.*, 2022, **53**, 238–253.

39 D. Kundu, B. D. Adams, V. Duffort, S. H. Vajargah and L. F. Nazar, A high-capacity and long-life aqueous rechargeable zinc battery using a metal oxide intercalation cathode, *Nat. Energy*, 2016, **1**(10), 16119.

40 H. Pan, Y. Shao, P. Yan, Y. Cheng, K. S. Han, Z. Nie, C. Wang, J. Yang, X. Li, P. Bhattacharya, K. T. Mueller and J. Liu, Reversible aqueous zinc/manganese oxide energy storage from conversion reactions, *Nat. Energy*, 2016, **1**(5), 16039.

41 T. Xiong, Z. G. Yu, H. Wu, Y. Du, Q. Xie, J. Chen, Y. W. Zhang, S. J. Pennycook, W. S. Lee and J. Xue, Defect engineering of oxygen-deficient manganese oxide to achieve high-performing aqueous zinc ion battery, *Adv. Energy Mater.*, 2019, (14), 1803815, DOI: **10.1002/aenm.201803815**.

42 T. T. Lv, Y. Y. Liu, H. Wang, S. Y. Yang, C. S. Liu and H. Pang, Crystal water enlarging the interlayer spacing of ultrathin $V_2O_5{\cdot}4VO_2{\cdot}2.72H_2O$ nanobelts for high-performance aqueous zinc-ion battery, *Chem. Eng. J.*, 2021, **411**, 128533.

43 J. Ding, Z. Du, B. Li, L. Wang, S. Wang, Y. Gong and S. Yang, Unlocking the potential of disordered rocksalts for aqueous zinc-ion batteries, *Adv. Mater.*, 2019, **31**(44), 1904369, DOI: **10.1002/adma.201904369**.

44 T. Holstun, T. P. Mishra, L. Huang, H. M. Hau, S. Anand, X. Yang, C. Ophus, K. Bustillo, L. Ma, S. Ehrlich and G. Ceder, Accelerating the Electrochemical Formation of the δ Phase in Manganese-Rich Rocksalt Cathodes, *Adv. Mater.*, 2025, **37**(6), 2412871, DOI: **10.1002/adma.202412871**.

45 Z. Cai, B. Ouyang, H. M. Hau, T. Chen, R. Giovine, K. P. Koirala, L. Li, H. Ji, Y. Ha, Y. Sun, J. Huang, Y. Chen, V. Wu, W. Yang, C. Wang, R. J. Clément, Z. Lun and G. Ceder, In situ formed partially disordered phases as earth-abundant Mn-rich cathode materials, *Nat. Energy.*, 2024, **9**(1), 27–36.

46 T. Li, T. S. Geraci, K. P. Koirala, A. Zohar, E. N. Bassey, P. A. Chater, C. Wang, A. Navrotsky and R. J. Clément, Structural Evolution in Disordered Rock Salt Cathodes, *J. Am. Chem. Soc.*, 2024, **146**(35), 24296–24309, DOI: **10.1021/jacs.4c04639**.

47 X. Chen, W. Li, Y. Xu, Z. Zeng, H. Tian, M. Velayutham, W. Shi, W. Li, C. Wang, D. Reed, V. V. Khramtsov, X. Li and X. Liu, Charging activation and desulfurization of MnS unlock the active sites and electrochemical reactivity for Zn-ion batteries, *Nano Energy*, 2020, **75**, 104869.

48 K. Dai, J. Wu, Z. Zhuo, Q. Li, S. Sallis, J. Mao, G. Ai, C. Sun, Z. Li, W. E. Gent and W. C. Chueh, High reversibility of lattice oxygen redox quantified by direct bulk probes of both anionic and cationic redox reactions, *Joule*, 2019, **3**(2), 518–541.

49 B. H. Gilbert, B. H. Frazer, A. Belz, P. G. Conrad, K. H. Nealson, D. Haskel, J. C. Lang, G. Srajer and G. De Stasio, Multiple scattering calculations of bonding and X-ray absorption spectroscopy of manganese oxides, *J. Phys. Chem. A*, 2003, **107**(16), 2839–2847, DOI: **10.1021/jp021493s**.

50 Y. Lin, Y. Hu, S. Zhang, Z. Xu, T. Feng, H. Zhou and M. Wu, Binder-free freestanding 3D Zn-graphene anode induced from commercial zinc powders and graphene oxide for zinc ion battery with high utilization rate, *ACS Appl. Energy Mater.*, 2022, **5**(12), 15222–15232, DOI: **10.1021/acsaem.2c02872**.

51 Z. Zhao, R. Wang, C. Peng, W. Chen, T. Wu, B. Hu, W. Weng, Y. Yao, J. Zeng, Z. Chen, P. Liu, Y. Liu, G. Li, J. Guo, H. Lu and Z. Guo, Horizontally arranged zinc platelet electrodeposits modulated by fluorinated covalent organic framework film for high-rate and durable aqueous zinc ion batteries, *Nat. Commun.*, 2021, **12**(1), 6606.

52 W. Li, K. Wang, S. Cheng and K. Jiang, An ultrastable presodiated titanium disulfide anode for aqueous "rocking-chair" zinc ion battery, *Adv. Energy Mater.*, 2019, **9**(27), 1900993, DOI: **10.1002/aenm.201900993**.

